Sound & Vibration 2025, 59(2), 2844.
https://doi.org/10.59400/sv2844

Article

How cavitation number shapes the kinetic mysteries of shoulder and tail cavitation in multi-medium vehicles

Hui Sun[1], Xianghong Huang[1,*], Zixuan Wang[2], Luyue Xi[1], Cong Gao[1], Lijia Yang[1]

[1] School of Naval Architecture & Ocean Engineering, Jiangsu University of Science and Technology, Zhenjiang 212001, China
[2] Shenyang Aircraft Design and Research Institute, Shenyang 110000, China
*** Corresponding author:** Xianghong Huang, huangxianghong@just.edu.cn

CITATION

Sun H, Huang X, Wang Z, et al. How cavitation number shapes the kinetic mysteries of shoulder and tail cavitation in multi-medium vehicles. Sound & Vibration. 2025; 59(2): 2844.
https://doi.org/10.59400/sv2844

ARTICLE INFO

Received: 25 February 2025
Accepted: 16 April 2025
Available online: 29 April 2025

Abstract: The underwater launch stability of multi-medium vehicles is critically challenged by the dynamic evolution of shoulder and tail cavitation bubbles, which generate asymmetric loads and compromise water-exit success rates. To address this, we designed a novel unconstrained underwater launch platform integrated with 3D-printed modular vehicle models (flat/round heads) and multi-modal sensing systems (high-speed cameras at 16,000 fps + triaxial accelerometers), enabling quantitative visualization of cavitation dynamics under controlled cavitation numbers (σ = 0.62–2.51). Critical findings reveal: Cavitation number governs development asymmetry—lower σ compresses shoulder bubbles longitudinally (maximum L = 1.8D at σ = 0.62 vs. 1.2D at σ = 2.51), while higher σ promotes lateral expansion (W peaks at 0.82D). Collapse-induced instability mechanisms—pressure oscillations within bubbles trigger nonlinear collapses (30% higher collapse velocity at σ = 0.62), generating asymmetric forces that amplify yaw deviations by 15%–22%. Tail cavity dual-phase dynamics—at σ < 1.38, tail bubbles exhibit secondary detachment with umbrella-shaped collapse (velocity rebound ΔV = 1.2 m/s), whereas σ > 2.51 induces early necking at launch tubes, reducing effective thrust by 40%. These findings establish quantitative relationships between σ and bubble-mediated instability, providing design guidelines for cavitation-resistant vehicle profiles and adaptive launch control systems. The experimental framework offers a cost-effective alternative to prototype testing, reducing development costs by 60% through scalable 3D-printed models.

Keywords: transmedia vehicle; hydrodynamic instability; bubble dynamics; asymmetric collapse; underwater launch stability

1. Introduction

To enhance the success rate of multi-medium vehicle launches, understanding the dynamics of shoulder/tail cavitation and their interaction with the vehicle is critical. Underwater cavitation formation and collapse directly impact structural loads and navigation stability. Prototype experiments offer intuitive results and valuable data for high-speed vehicle development, serving as a benchmark for theoretical and numerical models. However, their large-scale models, stringent launch conditions, high equipment demands, and costly material processing/sensor deployment make them resource-intensive and technically challenging. Consequently, scalable model experiments have become the mainstream approach, enabling prototype predictions through similarity laws.

The collapse of a cavitation bubble is influenced by its proximity to solid surfaces, shear flow, and ambient pressure conditions. Numerical research showed bubbles near oscillating boundaries collapse asymmetrically from boundary-induced

pressure variations [1]. A study revealed shear stress in flow amplifies bubble collapse asymmetry, boosting wall impact forces [2]. Studies reveal bubble cluster interactions significantly modify collapse strength, with group behavior amplifying or weakening effects depending on spacing and initial conditions [3]. Simulations show a collapsing bubble's shock waves affect nearby bubbles, causing secondary collapses and energy redistribution [4]. Gas layers near boundaries change bubble collapse behavior. Experiments show adherent gas layers lower collapse-induced peak pressure, reducing erosion risk [5,6]. Numerical studies further reveal that gas layers act as a buffer, dissipating shock wave energy and modifying collapse-induced jet formation [7]. Simulations reveal oscillating walls distort bubble collapse, generating directional jets and asymmetric shock waves [8]. Similarly, cavitation bubbles collapsing near rigid walls generate strong outgoing shock waves, affecting surrounding fluid dynamics [9]. Bubble bursts create sound waves useful for ultrasound cleaning and medicine. Studies find tiny bubbles make high-pitched noises when they pop [10]. Research shows rapid heat diffusion occurs during bubble growth and collapse, useful for sustainable tech [11]. Research on bubble collapse improves materials, medicine, and machines. Also explore uses in eco-friendly tech like water treatment [12].

Underwater cavitation impacts multi-medium vehicle stability. Studies on underwater gun launches examined gas curtain effects through fluid simulations. Results showed gas bubbles influence launch performance and flow stability, helping optimize underwater systems [13]. The study shows that firing underwater projectiles one after another creates flow disturbances, reducing their stability [14]. The study used simulations to show that air films forming around submarine-launched vehicles improve their aerodynamics [15]. Numerical simulations of underwater launches showed projectile shape affects flow dynamics and performance [16]. CFD simulations revealed how underwater firing's flow changes affect artillery stability and performance, aiding design optimization [17]. Their study of gas-liquid interactions during firing revealed these dynamics are crucial for optimizing underwater gun designs and multi-shot efficiency [18]. Cavitation interference significantly increases impact loads and alters projectile dynamics in successive underwater launches [19]. The pulsation characteristics of tail cavities under vertical launching conditions concluded that the dynamics of these cavities significantly influence launch stability and performance [20]. Numerical simulations show muzzle bubble dynamics during underwater launching significantly impact launch efficiency and performance [21]. Simulations showed the trans-medium UAV design enhances kinematic stability in both air and water [22]. This paper demonstrated that interactions between wake vortices can alter the trajectories and affect the performance of each projectile [23]. The research concluded that bubble asymmetry significantly affects projectile stability and performance [24]. Research revealed cavitation critically impacts load distribution and performance in underwater-launched vehicles [25]. Experiments and simulations showed bubble dynamics significantly impact underwater launch performance in high-speed cylinder interactions [26]. Research found that outlet cavity flow characteristics during underwater launching significantly affect launch performance [27].

However, these works largely neglect the synergistic interactions between multiple bubbles (e.g., shoulder and tail cavitation) in complex flow fields. While

these models frequently rely on idealized boundary conditions, they underestimate the stochastic pressure oscillations observed in physical experiments. To bridge these gaps, three key advancements are introduced. A scalable, unconstrained underwater launch platform is developed, including the integrates 3D-printed vehicle models with configurable head geometries (flat/round) and diameters (40 mm). This approach overcomes the cost and scalability limitations of prototype testing while maintaining geometric similarity. By synchronizing high-speed Phantom cameras (16,000 fps) with triaxial accelerometers, the paper achieved simultaneous visualization and quantitative analysis of bubble kinematics (e.g., aspect ratio L/W) and vehicle motion dynamics, a capability absent in prior scaled experiments. A dimensionless parameter is proposed to quantify cavitation initiation difficulty, correlating vehicle displacement and diameter under controlled σ conditions (0.62–2.51). This metric addresses the oversimplification of initiation criteria in existing studies.

2. Experiment set-up

2.1. Launch system

To investigate the influence of the cavitation number on the dynamic characteristics of shoulder and tail cavitation in multi-medium vehicles and to visualize the movement of underwater cavitation bubbles, an unconstrained underwater launch platform was designed and constructed, as shown in **Figure 1**. The experimental platform mainly consists of a launch system, data acquisition system, and experimental vehicle model. The water tank has a height of 2 m, a width of 1 m, a water depth of 1.5 m, and the launch tube is 1.5 m long.

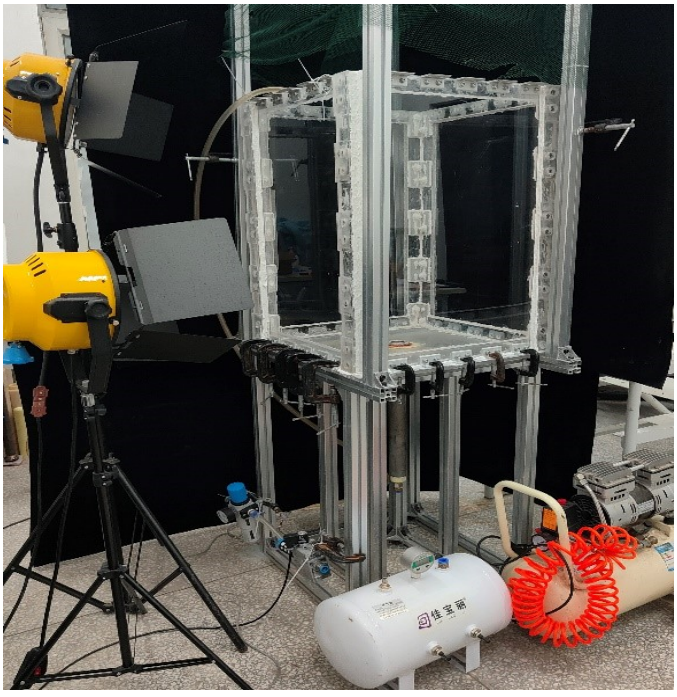

Figure 1. Underwater unconfined launch platform.

The launch system is illustrated in **Figure 1** and mainly consists of an air compressor, a safety air storage cylinder, an electromagnetic valve, a silencer, and a

PLC control integration box. The purpose of this system is to compress air using the air compressor and store it in the safety air storage cylinder. The electronic pressure gauge on the cylinder can display the internal air pressure in real time. The PLC control integration box is used to control the on and off timing of the electromagnetic valve in the gas supply pipeline of the storage cylinder. When the electromagnetic valve is opened, the high-pressure gas in the pipeline propels the vehicle out of the launch tube.

The air compressor selected from the OUTSTANDING company features an 800 W copper wire motor, as shown in **Figure 2**. Its maximum pressure can be adjusted up to 0.8 MPa, with a speed of 1380 r/min and a discharge volume of 60 L/min. For safety reasons and to prevent damage to the projectile model from excessive pressure, the maximum pressure of the air compressor should not exceed 0.5 MPa. To meet experimental needs, the purchased safety air tank has been modified.

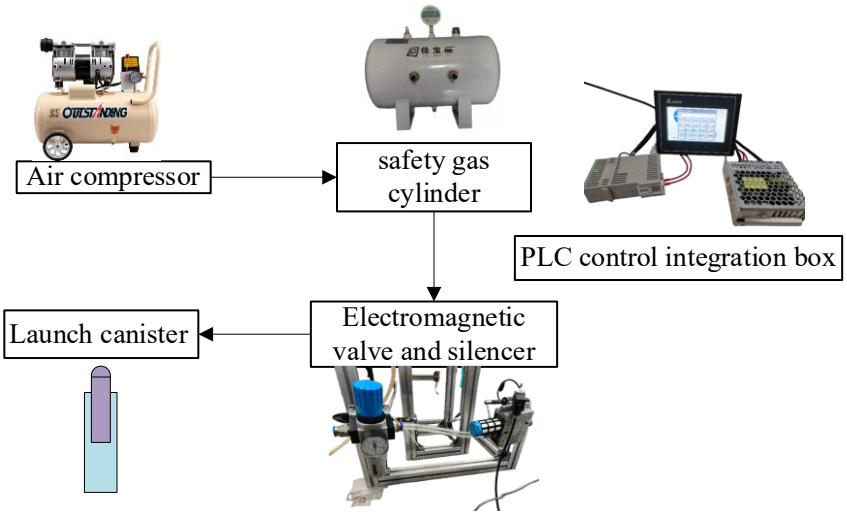

Figure 2. Launch system.

The role of the image data acquisition system is to visually capture the changes in cavitation during the movement of the navigating body. In this experiment, the high-speed camera used is the Phantom EVO710, set to a resolution of 512 × 800 and a maximum frame rate of 16,000 fps. Two high-speed cameras are positioned directly in front of the launch box to film the two phases of the navigating body: from exiting the tube to underwater movement, and from underwater movement to leaving the free liquid surface.

2.2. Experimental model

The experimental model is shown in **Figure 3**. It features a segmented design, consisting of a head section, a middle section, and a tail section, all manufactured using 3D printing. The model is made of polylactic acid (PLA), which has excellent impact toughness, wear resistance, good dimensional stability, and a wide temperature range for use. During experiments, a rubber sealing ring is placed at the step, and sealing tape is tightly wrapped around the joint to achieve a watertight effect. To investigate the influence of different head shapes on the cavitation characteristics of the vessel during motion, two different head models were designed: a round head and a flat head. The length of the head section is 50 mm, the middle section is 120 mm, and the tail

section is 30 mm, with an overall model diameter of 40 mm and a total length of 200 mm. Considering that the flat head model exhibits better shoulder cavitation effects, shoulder cavitation experiments will be conducted using the flat head model. Similarly, the round-head model, which is expected to perform better for tail cavitation effects, will be used for tail cavitation experiments.

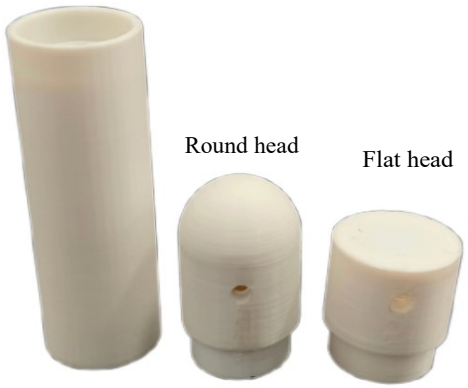

Figure 3. Experimental model.

2.3. Experimental procedure

The experimental procedure for the underwater unconstrained launch experiment is divided into three steps:

(1) Preparation before the experiment: the water in the launch box is filled to the specified level. The acceleration sensor and weight block are installed inside the model.

(2) The air compressor is started to store air in the safety storage tank; the air compressor is closed once the pressure gauge above the tank reaches the set pressure.

(3) The high-speed camera is turned. Then the electromagnetic valve is turned on, and the model launches smoothly from the launch tube.

For the issues that need to be studied in this paper, the experimental conditions have been designed. Since the cavitation number is the most important factor affecting the effectiveness of the underwater launch test, the test case contains both large and small cavitation numbers.

Cavitation number is defined as shown in Equation (1):

$$\sigma = \frac{p_\infty - p_v}{\frac{1}{2}\rho V_\infty^2} \tag{1}$$

The main parameters in Equation (1) are as follows:

p_∞ is the incoming pressure of the liquid;

p_v is the saturated vapor pressure of the liquid at ambient temperature;

ρ is the density of the liquid;

V_∞ is the speed of the vehicle when leaving the barrel in this paper.

In this experiment, the cavitation number was adjusted by adjusting the launch pressure to change the velocity of the vehicle to exit the cylinder. The parameters of the experimental conditions are shown in **Table 1**.

Table 1. Experimental conditions.

Working Condition No.	Nautical body head shape	Nautical Body Diameter (mm)	Cavitation number
1	crew cut	40	2.51
2	crew cut	40	1.38
3	crew cut	40	0.78
4	crew cut	40	0.62
5	roundhead	40	2.51
6	roundhead	40	1.38
7	roundhead	40	0.78
8	roundhead	40	0.62

3. Influence of cavitation number on the kinetic characteristics of shoulder cavitation

It is worth noting that for trans-medium vehicle model experiments, the cavitation number is the most critical parameter. The cavitation number is a crucial similarity parameter in the development of cavitation, significantly affecting the four stages of cavitation: inception, development, collapse, and shedding. Therefore, the following research focuses on a blunt-nosed body to investigate the changes in cavitation characteristics of the shoulder cavitation under different cavitation numbers.

The development of the shoulder cavity over time is shown in **Figure 4**. From the figure, it can be seen that the shoulder cavity of the flat-headed hull experiences four identical stages under different cavitation numbers: growth, development, collapse, and shedding. There are significant differences in the cavitation phenomena at each stage for different cavitation numbers. At the cavitation number = 2.51, during the t_1~t_2 period, no cavitation occurs at the shoulder of the flat-headed hull. However, under other medium and small cavitation number conditions, the shoulder cavity has already begun to form by t_2, and the smaller the cavitation number, the more intense the cavitation at t_2. At the moment of t_3, the shoulder cavitation in the initial and continuous development stage has an obvious downward slip phenomenon, and the shoulder cavitation is in the shape of a ring, and it is analyzed that when the cavitation number is large, the shoulder cavitation formed is cavitated more smoothly, with lower energy and mass, and the degree of dependence on the outer wall of the navigational body is weaker, which is easy to be affected by the influence of incoming currents and slides downward. In addition, by comparing and analyzing the morphology of the shoulder cavitations at the same moment in each figure, it can be found that when the cavitation number is larger, the shoulder cavitations are more inclined to develop horizontally, and the whole shows a short and wide morphology, while when the cavitation number is large, the shoulder cavitations are more inclined to develop vertically, and the whole shows a long and narrow morphology. At t_7, the shoulder cavitation has a small number of vesicular cavitations mixed with the water medium and the formation of cloud cavitations, but they did not fall off and continue to follow the main cavitation's upward movement. When the cavitation is 0.62 at t_7, the shoulder cavitation from the center has collapsed, and due to the small cavitation number, the downstream speed is larger; the collapse of the formation of the cloud cavitation no

longer follows the main cavitation, but the formation of the incoming flow is quickly wrapped in the downward movement.

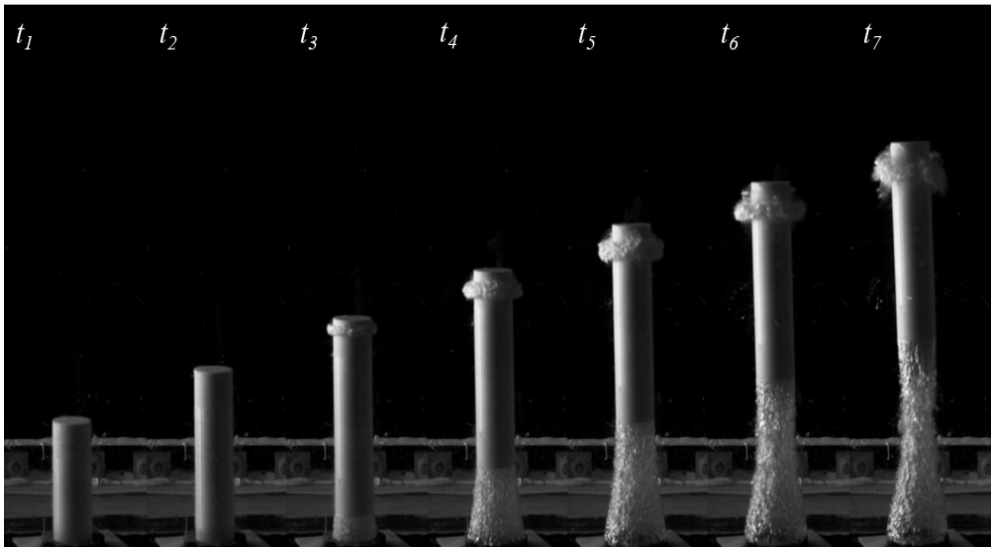

(a) Cavitation number = 2.51.

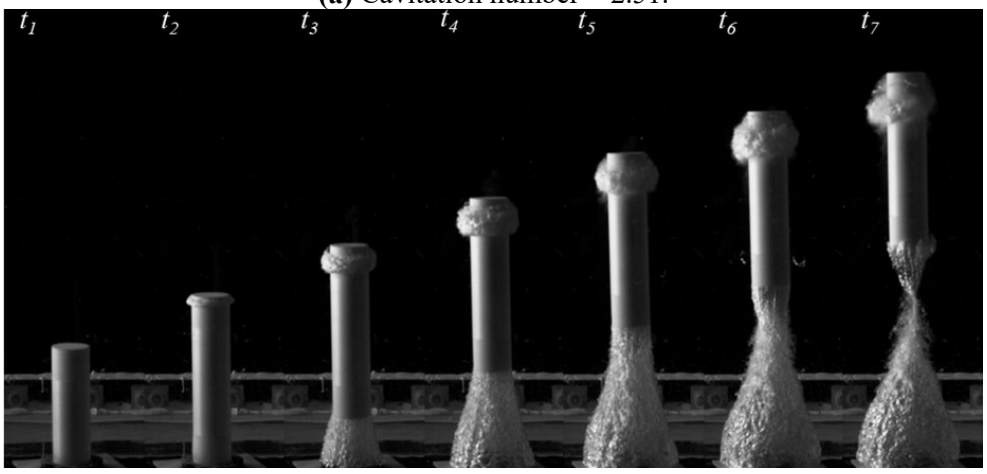

(b) Cavitation number = 1.38.

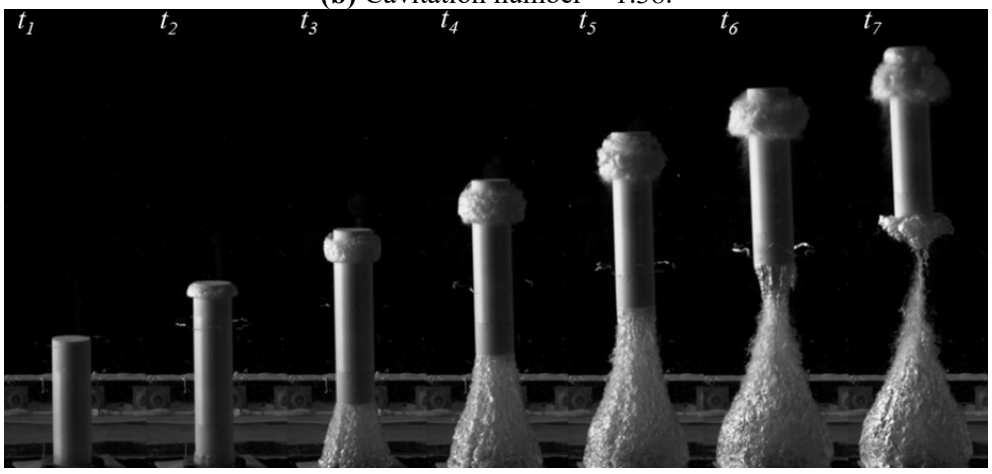

(c) Cavitation number = 0.92.

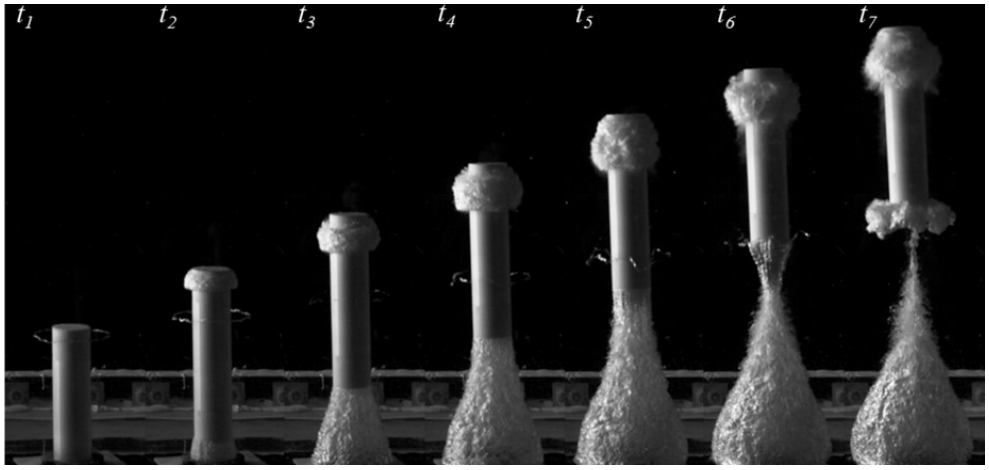

(d) Cavitation number = 0.78.

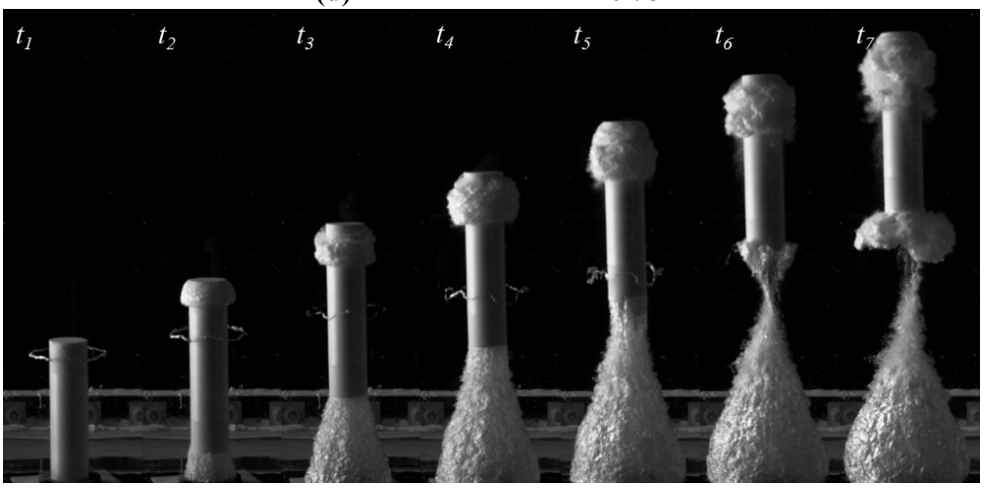

(e) Cavitation number = 0.62.

Figure 4. Shoulder cavitation motion process under different cavitation numbers (t_1 = 150/Δt, t_1 = 150/Δt, t_2 = 200/Δt, t_3 = 250/Δt, t_4 = 300/Δt, t_5 = 350/Δt, t_6 = 400/Δt, t_7 = 450/Δt, where Δt = 16,000). **(a)** motion process when Cavitation number = 2.51; **(b)** motion process when Cavitation number = 1.38; **(c)** motion process when Cavitation number = 0.92; **(d)** motion process when Cavitation number = 0.78; **(e)** motion process when Cavitation number = 0.62.

As shown in **Figure 4**, it can be observed that the motion of the multi-medium vehicle leads to a reduction in pressure oscillations within the flow field, thereby inducing the formation of shoulder cavities. However, the decrease in the vehicle's speed reduces the energy required to sustain the development of shoulder cavities, causing continuous oscillations of the shoulder cavities in the flow field. Variations in flow field pressure, combined with the motion of the multi-medium vehicle, result in rapid pressure changes within the shoulder cavities, leading to nonlinear oscillations. These nonlinear oscillations contribute to the asymmetric growth and collapse of the shoulder cavities. The asymmetric collapse of the shoulder cavities exerts uneven forces on the multi-medium vehicle, exacerbating its navigational deviation and ultimately causing the failure of the multi-medium vehicle during water exit.

In addition to the image data captured by the high-speed camera of the changes in the morphology of the cavitation during the motion of the sailing body, the kinetic characteristics of the shoulder cavitation can also be analyzed through the

measurement of the dimensions of the bubble length and width of the shoulder cavitation, and the measurement method of the bubble length and width of the shoulder cavitation set up independently is shown in the schematic diagram in **Figure 5**.

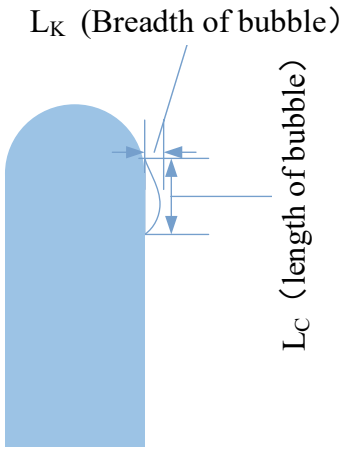

Figure 5. Schematic diagram of the shoulder cavitation length and width.

The changes in the length and width of the shoulder cavitation bubble of the flat-headed hull over time are shown in **Figure 6a**,**b**. From the graph of bubble length variation, it can be observed that for different cavitation numbers, the length of the shoulder cavitation bubble first increases to a maximum value and then decreases. This is because after reaching the maximum value, some of the bubbles coalesce to form a cloud of cavitation and detach. The bubble width variation graph indicates that under small cavitation number conditions, the bubble width of the shoulder cavitation first decreases and then increases rapidly. This occurs because, after a period of high-speed motion of the flat-headed hull, the dual resistance from the incoming flow and the formed shoulder cavitation gradually reduces the motion speed, leading to a decrease in the intensity of cavitation. As a result, the bubble width initially decreases; however, the jet generated by the tail cavity of the flat-headed hull creates a secondary impact at the tail, causing the motion speed to increase rapidly, which in turn increases the width of the shoulder cavitation bubble. The variation of the shoulder cavitation aspect ratio γ_j over time for different cavitation numbers is shown in **Figure 6c**. The shoulder cavitation aspect ratio is obviously much lower than the other conditions when the cavitation = 2.51, and the cavitation morphology shows a flattened ring, while the shoulder cavitation is more elongated under the small cavitation number.

The scatter plot in **Figure 7** shows the maximum values of bubble length and width of the shoulder cavity extracted under different cavitation numbers. It can be seen from the figure that the maximum bubble length increases with the decrease of the cavitation number. However, the maximum value of the shoulder cavity bubbles at larger cavitation numbers is greater than that in some conditions with smaller cavitation numbers. This indicates that shoulder cavity bubbles at larger cavitation numbers tend to develop laterally, suggesting that the cavitation number can influence the development trend of the shoulder cavity bubbles.

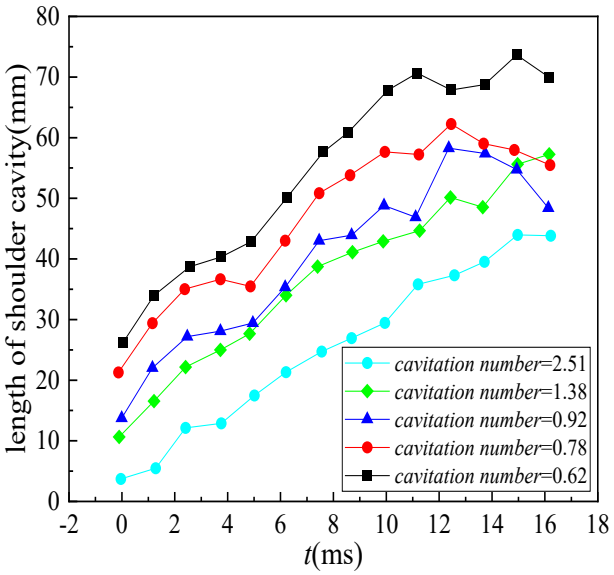

(a) Shoulder cavitation length.

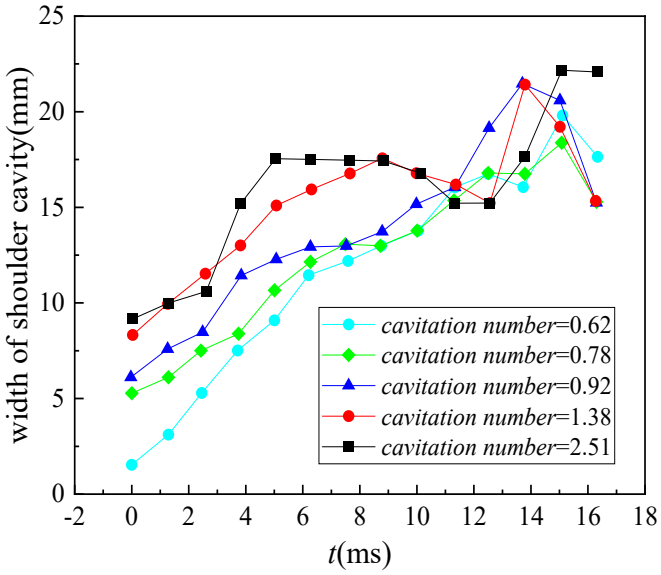

(b) Shoulder cavitation width.

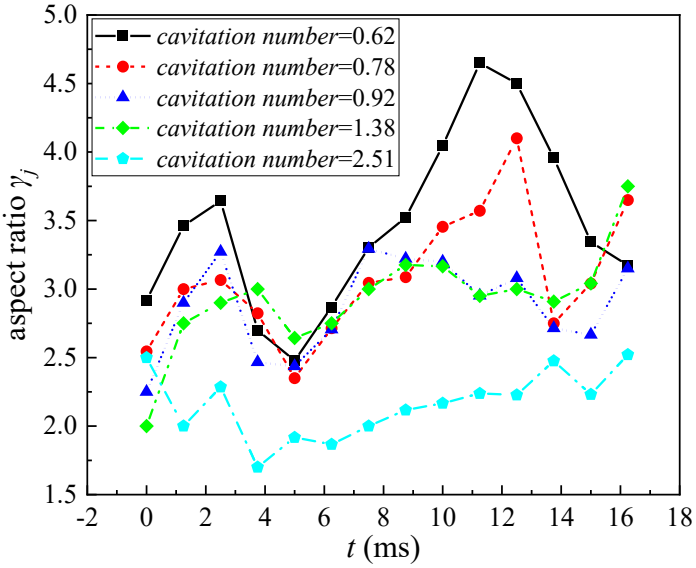

(c) Shoulder cavitation aspect ratio.

Figure 6. Effect of cavitation number on shoulder cavitation morphology. **(a)** effect on shoulder cavitation length; **(b)** effect on shoulder cavitation width; **(c)** effect on shoulder cavitation aspect ratio.

Under different parameter conditions, the time and degree of difficulty of the cavitation phenomenon occurring after the body is discharged from the cylinder are different. In order to facilitate the comparison of the cavitation characteristics of different sizes of the body and the body under different working conditions, a dimensionless parameter C_k is proposed as shown in Equation (2).

$$C_k = \frac{H_{\max}}{D_h} \tag{2}$$

where C_k denotes the degree of difficulty of the incipient cavitation phenomenon of the body, $H_{\max}$ denotes the maximum height of the highest point of the head of the

body from the mouth of the launch tube when the body reaches the same incipient cavitation state, and D_h denotes the diameter of the body.

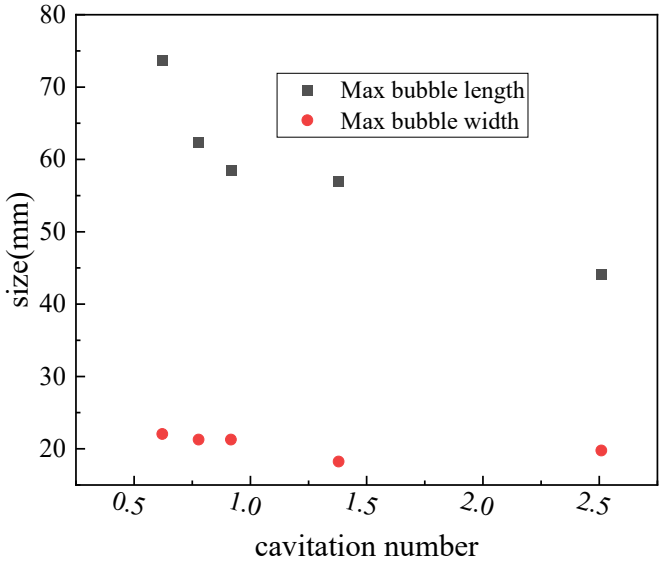

Figure 7. Variation of maximum shoulder cavitation length and width at different cavitation numbers.

The influence of different cavitation numbers on the incipient cavitation phenomenon of flat-head navigational bodies is shown in **Figure 8**. The smaller the cavitation number, the earlier the moment of shoulder cavitation incipient, and the easier the cavitation occurs. However, compared with the range of influence of air nuclei on incipient cavitation, the degree of influence of the cavitation number on incipient cavitation is smaller.

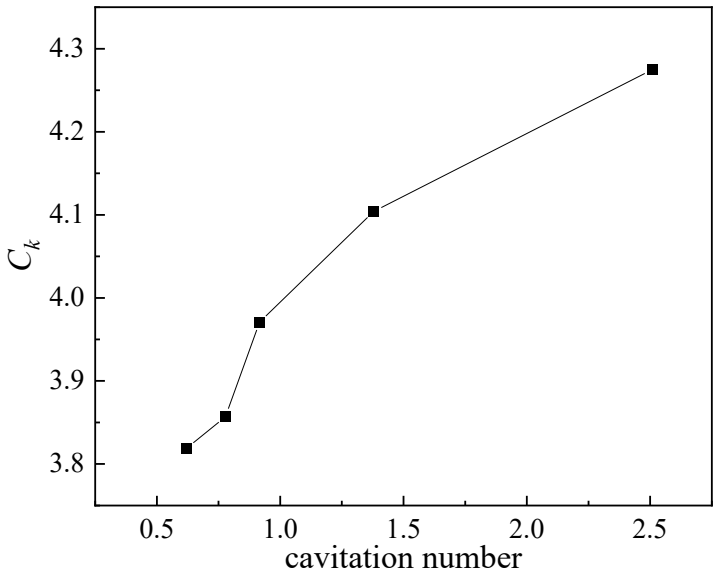

Figure 8. Effect of cavitation number on incipient cavitation of the navigational body shoulder cavitation.

4. Influence of cavitation number on the hydrodynamic properties of tail cavitations

In the transmedia body prototype experiment, the fuel dosage will be adjusted according to the different launching water depths to ensure that the body can leave the water smoothly according to the preset speed and state. In the model experiments, different water depths and different fuel dosages can be simulated by changing the cavitation number, so the evolution of the tail bubble of the navigational body under different cavitation numbers will be analyzed and studied by taking the round-ended navigational body as an example.

The experimental results show the development of the tail cavitation with time, as shown in **Figure 9**. From **Figure 9a**, it can be seen that when the cavitation number is 2.51, the navigational body can approximately simulate the motion of the prototype experiment when launching in shallow water depth with less fuel, which is significantly different from the motion process and the change of the cavitation morphology of the navigational body under other small cavitation numbers. During the expansion of the tail bubble, its vertical expansion speed is greater than its radial expansion speed, resulting in a cylindrical shape for the tail bubble. Unlike the necking and tearing phenomena that occur at a distance from the launch tube's nozzle for mid- and small-cavitation number flows, at larger cavitation numbers, the trailing cavity experiences tearing and breaking right at the nozzle of the launch tube. Moreover, the upper segment of the broken trailing cavity does not immediately generate a backflow impact on the tail of the vehicle; instead, it maintains an inverted conical shape, widening upwards while moving upwards attached to the tail of the vehicle. The lower segment of the broken trailing cavity does not exit the tube but rather remains within the launch tube and moves downward, forming a partially detached bubble cluster between the upper and lower segments of the trailing cavity. The lower segment of the tail cavity did not exit the tube but moved downward within it because the cavity exerts tension, pulling the upper end of that segment inward. Once the high-pressure gas barrier is broken near the tube opening, the fluid in the launch chamber flows in from the tube opening. The lower segment of the tail cavity then experiences pressure from the incoming fluid, causing it to move downward. At moments t_4~t_6, the tail cavity following the vehicle rapidly rises from the lower end due to tension, creating a rebound jet. This rebound jet causes the cavitation within the tail cavity to collapse from bottom to top, leading to a phenomenon of cavitation overflow. When the rebound jet reaches the tail of the vehicle, a swirling vortex forms at the lower end of the tail cavity, causing a reduction in its movement speed. At moments t_7~t_8, the vehicle begins to emerge from the water at the front, resulting in a secondary detachment of the tail cavity, leaving only a small portion to support the vehicle's upward motion.

As shown in **Figure 9b**–**e**, the evolution laws of the tail cavitation of the navigational body under the small and medium cavitation numbers are similar, and there is an obvious difference with the special evolution law of the tail cavitation of the navigational body under the large cavitation number. The smaller the cavitation number, the larger the velocity of the body movement, the larger the energy stored in the tail cavitation, the more intense the perturbation of the peripheral flow field of the

body, and the earlier the tail cavitation occurs in the phenomena of necking, pulling, and overflowing. At moments t_3~t_5, the tail cavity ruptures and forms a tail recirculation flow from bottom to top. From the figure, it can be observed that as the cavitation number decreases, the outflow of the tail jet from the impact on the cavity becomes more vigorous, and the opacity of the detached gas mass also increases. This indicates that at smaller cavitation numbers, the movement of the vortices and other complex structures formed inside the tail cavity intensifies. At moments t_6~t_8, as the vehicle discharges water, the tail cavity experiences secondary detachment during the outflow process. With the decrease in the cavitation number, the length of the tail cavity that ultimately follows the rear of the vehicle after the secondary detachment becomes longer, and both the cavity volume and the intensity of cavitation also increase.

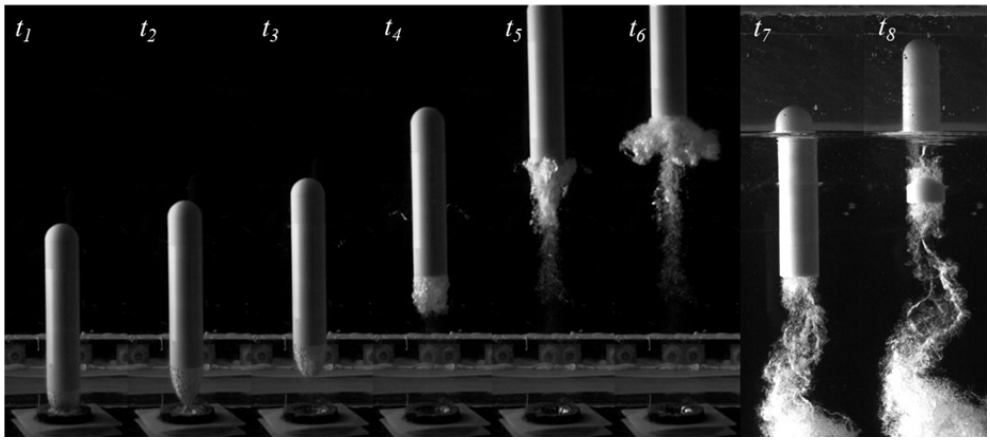

(a) Cavitation number = 2.51.

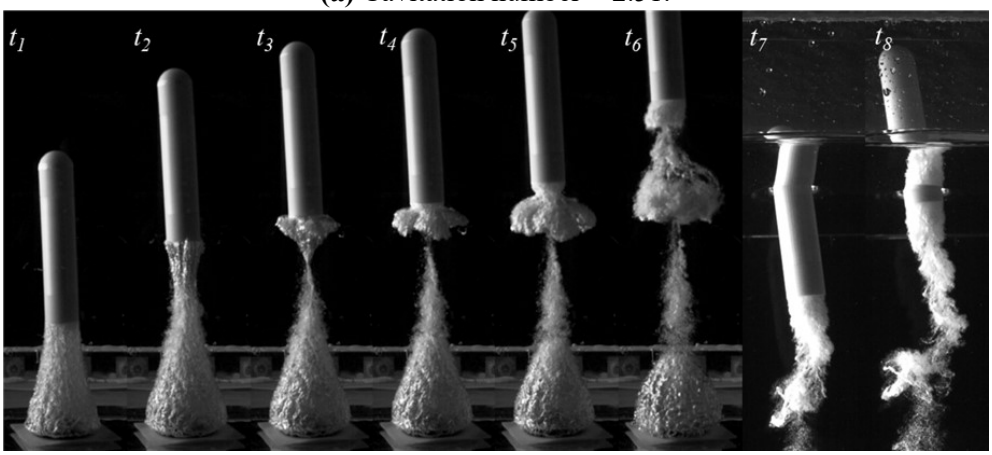

(b) Cavitation number = 1.38.

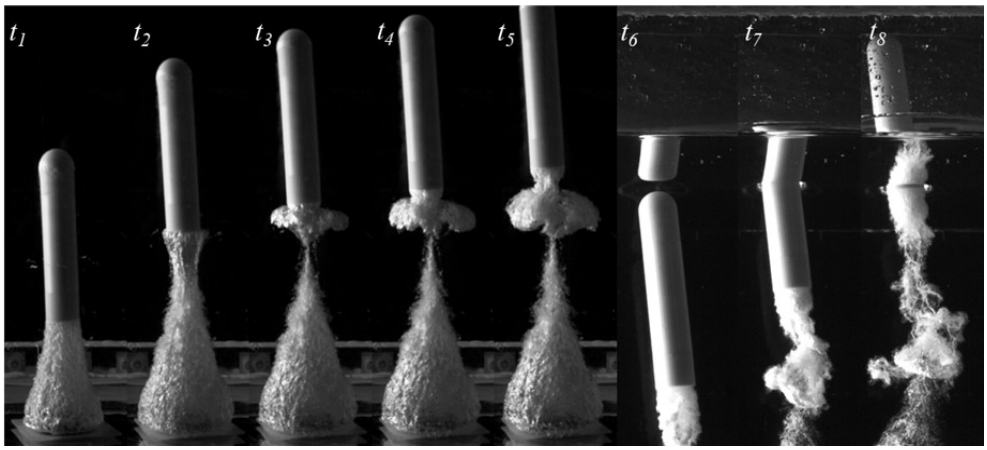

(c) Cavitation number = 0.92.

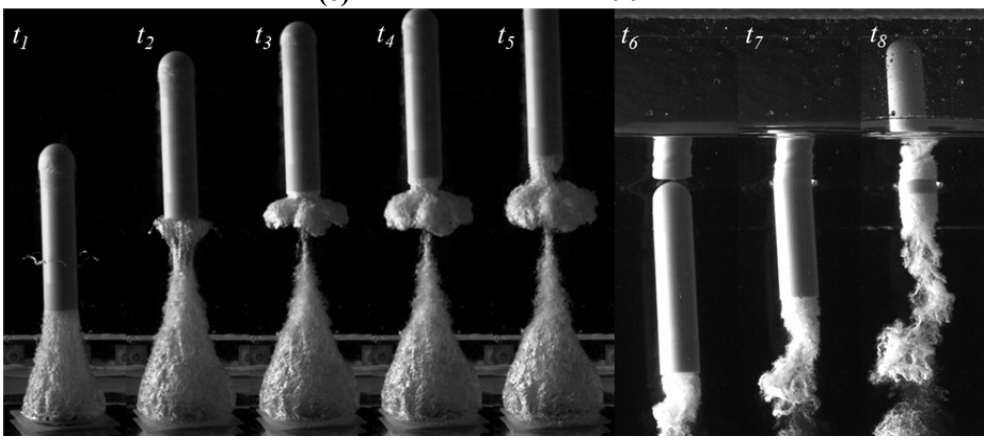

(d) Cavitation number = 0.78.

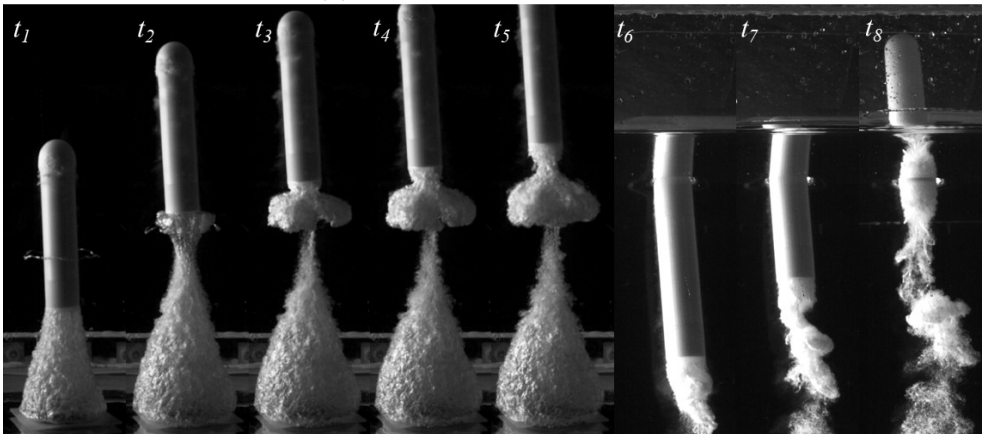

(e) Cavitation number = 0.62.

Figure 9. Underwater motion of the tail cavitation at different cavitation numbers (t_1 = 0/Δt, t_1 = 90/Δt, t_2 = 120/Δt, t_3 = 135/Δt, t_4 = 160/Δt, t_5 = 460/Δt, t_6 = 500/Δt, t_7 = 545/Δt, where Δt = 16,000). **(a)** motion process when Cavitation number = 2.51; **(b)** motion process when Cavitation number = 1.38; **(c)** motion process when Cavitation number = 0.92; **(d)** motion process when Cavitation number = 0.78; **(e)** motion process when Cavitation number = 0.62.

As shown in **Figure 10**, the tail cavity undergoes at least two cycles of development and collapse near the rear end of the multi-medium vehicle. During the first collapse, a large amount of gas adheres to the launch tube under tensile forces. As the vehicle moves, the pressure in the flow field at the rear end is lower than the static

pressure at the same depth, resulting in a small amount of gas clinging to the rear end of the vehicle and ascending with it. However, the asymmetric rupture of the tail cavity leads to uneven distribution of oscillatory pressure within the cavity. Consequently, the tail cavity exerts asymmetric forces on the vehicle, causing it to deviate from its intended course. The second collapse of the tail cavity occurs due to the combined effects of the vehicle's deviated motion and the depth-dependent variation in flow field pressure. These factors cause the internal pressure of the tail cavity to gradually exceed the external flow field pressure, while tensile forces exacerbate internal vibrations within the cavity until it ultimately collapses and detaches. The asymmetric vibrations during the collapse further amplify the uncertainty in the motion of the multi-medium vehicle.

In order to more accurately analyze the influence of each parameter on the evolution law of the caudal cavitation of the navigational body, firstly, we analyzed the change of its motion characteristics after the caudal cavitation was torn by necking, and we measured the length of the lower section, the length of the upper section, and the width of the upper section of the caudal cavitation after it was torn, and a schematic diagram of the measurement method for the caudal cavitation dimensions, which was set up by the independent, is shown in **Figure 10**.

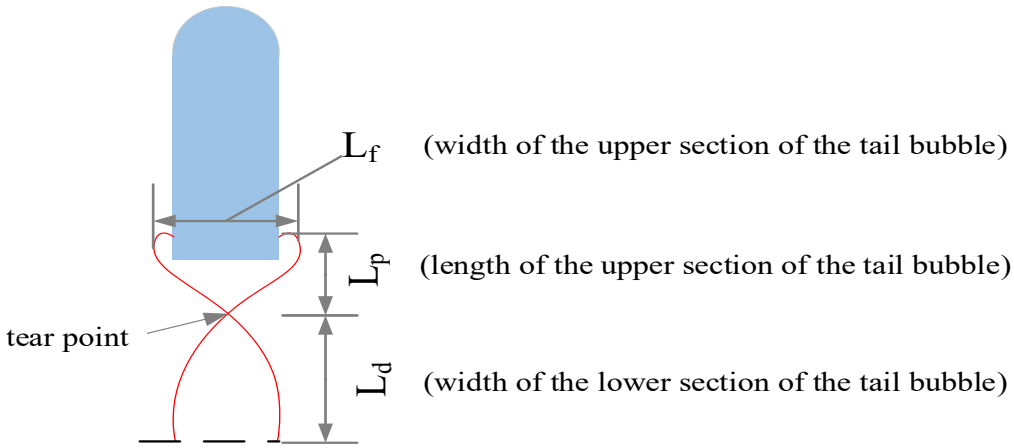

Figure 10. Schematic diagram for the dimensional parameters of the tailed cavitation.

The change in the size of the upper and lower segments of the tail cavitation when the tearing phenomenon occurs is shown in **Figure 11a**. From the diagram, it can be observed that, except for the upper segment length of the trailing cavity at high cavitation numbers being significantly greater than the lower segment length and experiencing tearing near the launcher nozzle, both mid and small cavitation numbers see the trailing cavity torn at a position further from the nozzle. Moreover, as the cavitation number increases, the total length of the trailing cavity and the length of the upper segment at the tearing point both increase, indicating that at small cavitation numbers, the length and volume of the cavity following the vehicle's tail increase, providing greater thrust to the vehicle. The proportion of the upper section of the tail cavitation in the total number of tail cavitations when the tail cavitation is torn is shown in **Figure 11b**. It can be seen from the figure that when the tail cavitation is torn in large cavitation numbers, the upper section of the tail cavitation that continues

to follow the body accounts for nearly 80% of the total length of the tail cavitation, whereas the upper section of the tail cavitation in the middle and large cavitation numbers accounts for only 20% of the total number of the tail cavitation.

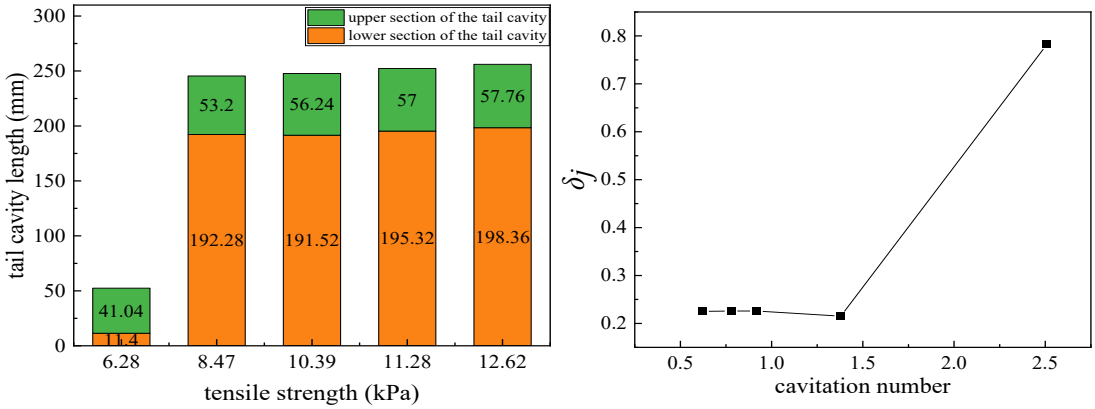

Figure 11. Characteristics of tail cavity size at different cavitation numbers. **(a)** Variation of tail cavitation dimensions with different cavitation numbers; **(b)** Plot of variation in the ratio of upper segment to total length of the caudal cavitation for different cavitation numbers length ratio of upper to total.

After the tail bubble is disrupted, the variations in length and width of the upper section of the tail bubble, which continues to follow the tail of the vehicle, are shown over time in **Figure 12**. From the graph depicting the changes in bubble length of the upper section of the tail bubble, it can be observed that under low and medium cavitation numbers, the length of the upper section of the tail bubble consistently decreases. However, under small cavitation number conditions, the length decreases to a minimum value before gradually increasing again. This behavior is due to the high speed of the vehicle; once the bubble collapses to its minimum length, it forms an umbrella-shaped bubble, which starts to detach, causing the bubble to stretch again. A portion of the umbrella-shaped bubble remains attached to the tail of the vehicle. The width of the upper section of the tail cavitation in the bubble width size change chart, the width of the upper section of the tail cavitation under the large cavitation number did not change, and the width of the upper section of the tail cavitation under the middle and small cavitation numbers gradually increased with the increase of time.

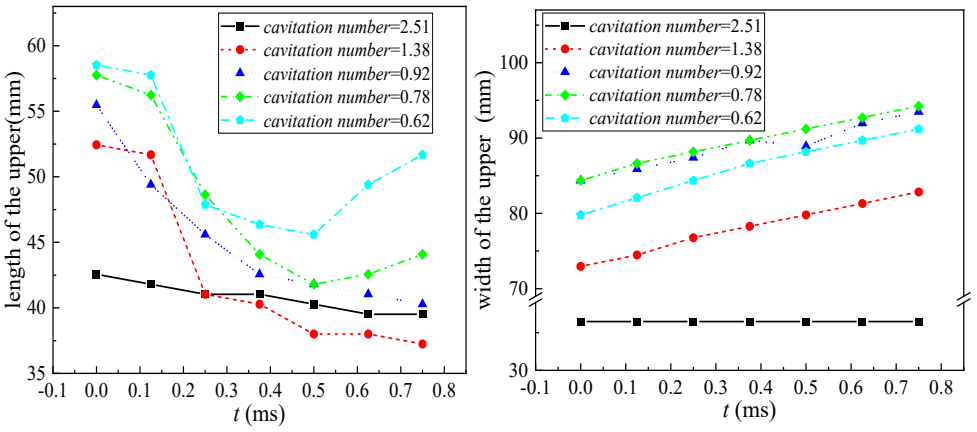

Figure 12. Dimensional changes of tail cavitation. **(a)** Variation of bubble length.; **(b)** Variation of bubble width.

5. Conclusion

This article explores the kinetic characteristics of shoulder and tail cavitation in a multi-medium vehicle during underwater launch experiments using an unconstrained underwater launch platform. The conclusions are as follows:

(1) The cavitation number significantly influences the occurrence and development of shoulder and tail cavitation, leading to asymmetrical loading on the vehicle, which affects its underwater motion at high angles and reduces the success rate of emergence.

(2) The cavitation number can alter the development trend of shoulder cavitation; its maximum bubble length generally decreases with larger cavitation numbers, but larger cavitation numbers promote lateral development, with maximum values at large cavitation numbers exceeding those at medium levels.

(3) A smaller cavitation number correlates with greater vehicle speed and reduced relative velocity between the tail cavitation and the vehicle, indicating a smaller impact of the tail cavitation on the rear of the vehicle.

(4) Pressure oscillation within the shoulder and tail cavities leads to cavity growth and collapse. The collapse-induced loads from cavity vibrations act asymmetrically on the bow and stern of the multi-medium vehicle, causing deviations in its underwater motion and amplifying the uncertainty of its water exit process.

Author contributions: Conceptualization, XH and HS; methodology, CG; software, ZW; validation, ZW, XH and HS; formal analysis, LX; investigation, LY; resources, XH; data curation, ZW; writing—original draft preparation, HS; writing—review and editing, XH; visualization, LX; supervision, CG; project administration, LY; funding acquisition, XH. All authors have read and agreed to the published version of the manuscript.

Funding: The present investigation is supported and funded by the National Natural Science and Foundation of China (Grant no.52401383, Grant no.52401368).

Acknowledgments: All of the help is greatly appreciated and acknowledged by the authors.

Institutional review board statement: Not applicable.

Informed consent statement: Not applicable.

Conflict of interest: The authors declare no conflict of interest.

References

1. Li JB, Xu WL, Xia Y, et al. Effect of an air bubble on the collapse shock wave of a cavitation bubble. Ocean Engineering. 2024; 297: 117094.
2. Aganin AA, Khismatullina NA, Nigmatulin RI. Pulse Impact on Cavitation Bubble Collapse. High Temperature. 2023; 61: 385–391.
3. Nguyen QT, Nguyen VT, Phan TH, et al. Numerical study of dynamics of cavitation bubble collapse near oscillating walls. Physics of Fluids. 2023; 35: 013306.
4. Zhan S, Duan H, Pan L, et al. Molecular dynamics simulation of shock-induced microscopic bubble collapse. Physical Chemistry Chemical Physics. 2021; 23: 8446–8455.

5. Li JB, Xu WL, Zhai YW, et al. Influence of multiple air bubbles on the collapse strength of a cavitation bubble. Experimental Thermal and Fluid Science. 2021; 123: 110328.
6. Liu J, Xiao W, Yao X. Pressure characteristics of a nonspherical underwater explosion bubble in a compressible fluid. Physics of Fluids. 2024; 36: 057145.
7. Sagar HJ, Lin Y, el Moctar O. Dynamics of a single cavitation bubble near an oscillating boundary. Scientific Reports. 2024; 14: 22031.
8. Bhola S, Rodriguez Jr M, Beig SA, et al. Inertial collapse of a gas bubble in a shear flow near a rigid wall. Journal of Fluid Mechanics. 2025; 1004
9. Rashid FL, Al-Obaidi MA, Hussein AK, et al. Bubble Dynamics in Sustainable Technologies: A Review of Growth, Collapse, and Heat Transfer. Processes. 2025; 13(1): 38.
10. Kim MZ. Energy Transport During Growth and Collapse of a Cavitation Bubble [PhD thesis]. University of Michigan; 2022.
11. Bao H, Reuter F, Zhang H, et al. Impact-driven cavitation bubble dynamics. Experiments in Fluids. 2023; 64: 27.
12. Han W, Xing Y, Li R, et al. Dynamic Characteristics of Near-wall Single Bubble Collapse-induced Shock Waves. Journal of Applied Fluid Mechanics. 2025; 18(3): 617–630.
13. Zhang X, Yu Y, Zhou L. Numerical study on the multiphase flow characteristics of gas curtain launch for underwater gun. International Journal of Heat and Mass Transfer. 2019; 134: 250–261.
14. Gao S, Shi Y, Pan G, Quan X. A study on the flow interference characteristics of projectiles successively launched underwater. International Journal of Multiphase Flow. 2022; 151: 104066.
15. Shi Y, Ren J, Gao S, Pan G. Numerical Investigation on Air Film Fusion of Pressure-Equalizing Exhaust around Shoulder Ventilation of Submarine-Launched Vehicle. Journal of Marine Science and Engineering. 2022; 10(1): 39.
16. Xue X, Zhang J, Yu Y. Muzzle flow field characteristics of underwater sealed launch system under different projectile shapes. Ocean Engineering. 2023; 285.
17. Zhang X, Yu Y, Zhang X. Numerical simulation and analysis of the 3D transient muzzle flow field of underwater artillery. Ocean Engineering. 2023; 284: 115270.
18. Zhang X, Yu Y, Zhang X. Research on multiphase flow field characteristics of underwater gun double-tube parallel firing. Propellants Explosives Pyrotechnics. 2023; 48(8): e202300068.
19. Gao S, Shi Y, Zhang S, Pan G. Research on the cavitation flow interference and impact loads of successively launched underwater projectiles. International Journal of Multiphase Flow. 2024; 178: 104878.
20. Ren Z, Wang X, Cheng S, et al. Numerical study on the pulsation characteristics of tail cavities under vertical launching conditions. Ocean Engineering. 2024; 305: 117948.
21. Sun Z, Li Q, Zhang X, et al. Muzzle bubble dynamics characterization of underwater launching. Physics of Fluids. 2024; 36: 085135.
22. Wei T, Lu D, Zeng Z, Lian L. Trans-Media Kinematic Stability Analysis for Hybrid Unmanned Aerial Underwater Vehicle. Journal of Marine Science and Engineering. 2022; 10(2): 275.
23. Shi Y, Gao S, Pan G, Quan X. Simulation of the wake vortex and trajectory characteristics of successively launched multiple projectiles. Ocean Engineering. 2022; 249: 110962.
24. Gao S, Shi Y, Pan G, Quan X. Research on the effect of asymmetric bubbles on the load characteristics of projectiles during an underwater salvo. Applied Ocean Research. 2022; 124: 103212.
25. Gao S, Shi Y, Pan G, Quan X. A study on the performance of the cavitating flow structure and load characteristics of the vehicle launched underwater. Physics of Fluids. 2022; 34: 125108.
26. Zhang S, Chen QH, Liu C, et al. Transient interactions between bubbles and a high-speed cylinder in underwater launches: An experimental and numerical study. Journal of Hydrodynamics. 2023; 35: 36–45.
27. Shi Y, Ren J, Gao S, et al. Simulation research on the outlet cavity features in the underwater launching process. Ocean Engineering. 2023; 267: 113278.